PAPER

Check for updates

Revisiting the structural, electronic and photocatalytic properties of Ti and Zr based perovskites with meta-GGA functionals of DFT

Waqas Zulfiqar,[a] Syed Muhammad Alay-e-Abbas, [ID] *[ab] Ghulam Abbas, [ID] [cd]
Amel Laref, [ID] [e] J. Andreas Larsson[b] and Ali Shaukat[f]

The strongly constrained and appropriately normed (SCAN) functional of density functional theory (DFT) conforms to all possible exact constraints required of a meta-GGA functional and offers good approximations for structural and energetic properties of solids in comparison to experiments. However, SCAN is unable to fully overcome the underestimation of band gap for perovskite oxide materials suitable for photocatalysis. In the present work, we use a combination of meta-GGAs SCAN and modified Becke–Johnson local density approximation (mBJ-LDA) potential functional to accurately compute the structural, energetic, mechanical, vibrational and optoelectronic properties of Ti and Zr based ABO_3 (A = Sr, Ba and B = Ti and Zr) perovskite oxides. In addition to evaluating their physical properties, the potential applications of these materials as photocatalyst operating in the UV region of the electromagnetic spectrum are also examined. We show that the structural, energetic, mechanical and vibrational properties calculated using SCAN are in better agreement with experimental data as compared to the commonly used semi-local functionals of DFT. However, the optoelectronic properties of the large band gap Ti and Zr based perovskite oxides are further improved if computed with the mBJ-LDA potential functional, whereby an even higher level of accuracy than with SCAN is achieved, with results that are comparable to the computationally expensive hybrid DFT functionals. On the whole, our DFT calculations indicate that a combination of SCAN and mBJ-LDA functionals for exploring the physical properties of large band gap perovskite oxides provide the means for identifying photocatalysts suitable for hydrogen production at low computational costs.

1. Introduction

In condensed matter physics and related sciences, Kohn–Sham (KS) density functional theory (DFT) has become a standard *ab initio* tool for exploring materials. For this reason DFT is being rigorously used for understanding the physical properties of materials and has proven to be particularly instrumental in predicting novel materials.[1–5] Since the precision of KS DFT

[a] *Computational Materials Modeling Laboratory, Department of Physics, Government College University, Faisalabad, 38040, Faisalabad, Pakistan. E-mail: syed.muhammad.alay-e-abbas@ltu.se, alayabbas@gcuf.edu.pk*

[b] *Applied Physics, Division of Materials Science, Department of Engineering Sciences and Mathematics, Luleå University of Technology, 97187 Luleå, Sweden*

[c] *School of Materials Science and Engineering, Hanshan Normal University, Chaozhou 521041, China*

[d] *College of Optoelectronic Engineering, Shenzhen University, Shenzhen 518060, China*

[e] *Department of Physics and Astronomy, College of Science, King Saud University, Riyadh, 11451, Saudi Arabia*

[f] *Department of Physics, Quaid-e-Azam Campus, University of the Punjab, Lahore, 54590, Pakistan*

calculations is strongly dependent on the selected approximation for computing exchange–correlation energy (*i.e.* $E_{xc} = E_x + E_c$), efforts for developing reliable functionals for determining E_{xc} have seen a steady progress.[3,6,7] By examining self-consistent one-electron equations, one expects that a universal exchange–correlation energy functional for KS DFT, wholly dependent on the ground-state electron density, ρ, can be obtained since $E_{xc}[\rho]$ is expressed by half of the Coulomb interaction in a double integral over space between electron and exchange–correlation hole. However, an approximate functional is always needed in real applications of KS DFT where semi-local approximations have traditionally allowed to formally compute $E_{xc}[\rho]$ from a single integral through a computationally efficient procedure.

Over the years, many DFT functionals have been developed which can be assigned to one of the four rungs of Jacob's ladder based on their level of sophistication and acquired accuracy.[8] Among these four rungs of Jacob's ladder of DFT functionals, the first three rungs are occupied by semi-local approximations.[8,9] A common feature of all the semi-local DFT functionals is that they can be expressed as single integral,

4862 | *J. Mater. Chem. C*, 2021, **9**, 4862–4876

This journal is © The Royal Society of Chemistry 2021

$E_{xc} = \int \varepsilon_{xc}(\rho) d^3r$, where ε_{xc} is the exchange–correlation energy density per volume. For the first and second rungs, respectively, ε_{xc} is expressed in terms of electron density, ρ, alone (as in the case of local density approximation (LDA))[10] and ρ and its first gradient, $\nabla\rho$, (as in the case of generalized gradient approximation (GGA)).[11] On the other hand, combining electron density and its first derivative with kinetic-energy density and/or $\nabla^2\rho$ gives us the so-called meta-GGA functionals, which occupy the third rung of Jacob's ladder.[7,9] Apart from the semi-local functionals, there also exist DFT functionals which allow computing $E_{xc}[\rho]$ through a double integral or Hartree–Fock (HF) exchange. Although accurate, these so-called hybrid functionals are computationally much more expensive than the semi-local functionals and thus occupy the fourth rung of the Jacob's ladder.[12]

Recently, meta-GGA functionals have been increasingly employed to compute physical properties of complex oxide semiconductors. This can mainly be attributed to the fact that earlier theoretical studies clearly show that the structural and energetic properties of these materials in general,[9,13] and optoelectronic properties of large band gap semiconductors in particular,[14] are not accurately predicted by LDA and GGA functionals. The quest for improving accuracy in determining the physical properties of perovskite oxides can partly be ascribed to their potential applications in advance oxidation processes (AOPs) for which various research groups are making efforts in designing new and efficient photocatalysts.[15,16] In this context, perovskite oxides having the chemical composition ABO_3 constitute a potential class of ceramic materials which are candidates for numerous device applications. This can mainly be ascribed to the presence of BO_6 octahedra where the electronic states of the B and O atoms play dominant roles in the conduction and valence band edges, respectively. Consequently, this provides huge opportunities to considerably alter the physical properties of these materials through chemical as well as physical means.[17,18] In particular, strontium titanate ($SrTiO_3$), barium titanate ($BaTiO_3$), strontium zirconate ($SrZrO_3$) and barium zirconate ($BaZrO_3$) are important perovskite oxides in which the 3d and 4d electrons of Ti and Zr, respectively, are bonded with the 2p electrons of oxygen. The d electrons introduced by the presence of transition metals in the titanium and zirconium based perovskite oxides bring about interesting physical properties for these materials which substantiate the exceptional importance of these materials. These materials have therefore been thoroughly studied both experimentally and theoretically in the past for a wide range of applications. In their pristine forms, both the titanates and zirconates of Sr and Ba show an insulating nature under ambient conditions that persists even at very high temperatures despite structural phase transitions. Owing to their chemical and mechanical stabilities at high temperature, these compounds have found applications in hydrogen sensors, fuel cells and electronic devices.[19–21] Importantly, there are several reports available in the literature which place these materials among the most suitable candidates for photocatalysis applications.[16] Owing to these facts, it is inevitable that an accurate account of the structural, energetic and optoelectronic

properties of ABO_3 (where A = Sr and Ba; B = Ti and Zr) perovskite oxides should be obtained using DFT calculations.

In 2015, Sun *et al.*[13] proposed the strongly constrained and appropriately normed (SCAN) meta-GGA functional, which conforms to all the known exact constraints for a meta-GGA. These include six constraints each for the exchange and correlation together with 5 constraints for the sum of the two.[13] In SCAN, the orbital kinetic energy densities of each spin are also added along with other ingredients (*e.g.* local spin density approximation (LSDA) and spin-density gradients) to obtain exchange and correlation energies, while the exchange and correlation potentials can still be computed using the Perdew–Burke–Ernzerhof (PBE) GGA.[11] As a result, structural and energetic properties computed using the SCAN functional show better accuracy for most types of bonds as compared to standard semi-local functionals of DFT.[22,23] In fact, the SCAN functional has proven to be more efficient than hybrid DFT for structural and energetic properties at only a fraction of the computational cost.[13,22,23] Despite these advantages, the under-estimation of band gaps and incorrect optical properties for transition metal oxides computed using SCAN still requires one to resort to either semi-empirical methods[23] or hybrid DFT calculations.[24,25] In order to remain truly *ab initio* and within the regime of meta-GGA functionals of DFT with low computational cost, it is intuitive to compute the optoelectronic properties of large band gap Ti and Zr based perovskite oxides by employing modified Becke–Johnson local density approximation (mBJ-LDA) functional proposed by Tran and Blaha[14] using the ground state structural properties obtained from SCAN functional. Motivated by this, in the present study we use a combination of SCAN and mBJ-LDA meta-GGA functionals for computing the structural, energetic, mechanical, vibrational, electronic and optical properties of ABO_3 (where A = Sr and Ba; B = Ti and Zr) perovskite oxides using the all-electron full-potential linearized augmented plane wave method (FP-LAPW) of DFT. As the compounds under study are potential candidates for photocatalysis,[16] we examine their photocatalytic properties for producing hydrogen through water splitting using the electronic properties computed with SCAN and mBJ-LDA functional. We expect that the results provided in this study would prove helpful in designing and improving the photocatalytic activities of the ABO_3 perovskite oxides in future studies.

2. Computational methods

In this work, the DFT calculations are performed using the WIEN2k package.[26] For the FP-LAPW method employed in the present work, the core and valence states are separated by muffin-tin spheres such that the electron wave function inside these spheres is augmented plane waves having spherical harmonics, while in the interstitial region the electron wave function is modeled using plane waves. The muffin-tin radii are chosen to be 2.1, 2.3, 1.8, 1.85. and 1.6 a.u. for Sr, Ba, Ti, Zr, and O atoms, respectively, while an energy separation of -6.0 Ry is used between the core and the valence states. With the present

This journal is © The Royal Society of Chemistry 2021

J. Mater. Chem. C, 2021, **9**, 4862–4876 | **4863**

choice of muffin-tin radii and energy separation between the core and valence states, the Sr (4s, 4p, 5s), Ba (5s, 5p, 6s), Ti (3s, 3p, 3d, 4s), Zr (4s, 4p, 4d, 5s) and O (2s, 2p) states are treated as valence states. For the interstitial region, the plane wave cutoff $R_O K_{max}$ (where R_O is the muffin-tin radius of oxygen and K_{max} is the largest **K** vector of the plane wave expansion) and the Fourier expansion of charge density vector G_{max} are set to be 8.0 and 24 Bohr^{-1}, respectively. For the case of cubic perovskite unit cell, 84 k-points in the irreducible wedge of the first Brillouin zone (corresponding to a $14 \times 14 \times 14$ k-mesh) are used and the energy and charge convergence criteria are set to 10^{-5} Ry and 10^{-3} e, respectively. During geometry optimization the atomic forces are always minimized to a value less than 1 mRy a.u.$^{-1}$ using the SCAN functional for obtaining ground state atomic positions.

Since SCAN has previously been shown to perform better in calculating structural and energetic properties of band gap materials as compare to other functionals,[13] it has been used for computing all the ground state geometries and energetic properties in this work. On the other hand, the electronic and optical properties are computed using both SCAN and mBJ-LDA functionals using the SCAN optimized structures, where improved parameters of mBJ-LDA for semiconductors proposed by Koller et al. are utilized.[27] Thus, we combine the good structure from SCAN with the good electronic structure of mBJ-LDA (i.e. SCAN//mBJ-LDA simulations), since the latter is a potential functional and cannot be used for computing structural properties.[14] It is worth pointing out here that the correlation energy and correlation potential parts of mBJ-LDA can be computed using the PBE GGA. Since the SCAN functional uses PBE GGA for the correlation potential,[13,26] one might desire the same parameterization scheme and perform SCAN//mBJ-GGA simulation of the electronic properties. However, we note that the electronic band structure computed using mBJ-GGA yield band gaps that are farther from experiment, compared to mBJ-LDA. This can be ascribed to the fact that parametric optimization[27] for this potential functional has only been carried out for the default exchange–correlation energy obtained from LDA[26] and can lead to alightly larger deviation in band gap values when used for mBJ-GGA calculations.

For the present study, we consider the prototype cubic crystal (space group No. 221, $Pm\bar{3}m$) structure of SrTiO$_3$, BaTiO$_3$, SrZrO$_3$ and BaZrO$_3$ perovskites and compute the structural properties using the SCAN functional. Since the energetic properties presented in this study also required computation of ground state properties of the oxygen molecule, elemental solids and binary oxides, all the structural parameters for these molecules and solids are also optimized using the SCAN functional. In the case of oxygen molecule, force minimization is performed for computing the optimized bond length. On the other hand, lattice parameters of elemental solids, binary oxides and ternary oxides are computed using self-consistent calculation for a series of fixed volumes of their respective unit cells. Where necessary, the c_0/a_0 and b_0/a_0 ratios have also been optimized. The SCAN optimized unit cells of all the ABO$_3$ compounds are subsequently used for computing the electronic and optical properties. For computing the mechanical properties, we have utilized the Elastic Constants for Cubic Cases (ELAS) program provided within the WIEN2k package.[26] For the computation of the vibrational properties of the ABO$_3$ compounds (using a 40-atom supercell), the frozen phonon approximation was employed using the phonopy code.[28] For all the calculations involving phonons, a force convergence criteria of 0.01 mRy a.u.$^{-1}$ was used. In order to eliminate numerical noise in our phonon calculations, the charge density grid has been enlarged by a factor of 2, while symmetrization of the force constants was also taken into account during post processing of the forces with the phonopy code.[29]

3. Results and discussion

3.1. Structural and energetic properties

Since thermodynamic quantities, such as enthalpy of formation, require one to find the difference between the cumulative total energies of atomic species in their stable reference phases and the total energies of the compounds constituted by these atoms, it is important that the exchange–correlation functional is able to provide good approximation of the ground state energies. For this reason, we first examine the performance of the SCAN functional in determining the energetic properties of all the atoms constituting the ABO$_3$ (where A = Sr and Ba; B = Ti and Zr) compounds. Table 1 presents the structural properties and cohesive energies of O$_2$ dimer, fcc Sr, bcc Ba, hcp Ti and hcp Zr computed using the SCAN functional. In the present work, we have computed the cohesive energy, E_c, as the difference between the total energy of the above-mentioned stable reference phases of an atom X and the energy of the same atom X placed inside a large supercell, i.e.

Table 1 Structural properties (Å) and cohesive energies (eV per atom) of oxygen molecule, face centered cubic unit cell of strontium, body centered cubic unit cell of barium, hexagonal closed packed unit cell of titanium and hexagonal closed packed unit cell of zirconium computed using the SCAN functional. For the sake of comparison, results of the GGA functional reported in previous DFT studies and experimental data are also presented

System	SCAN (this work)	GGA (previous DFT studies)	Experiment
O$_2$ (molecule)			
r_0	1.215	1.219[30]	1.210[31]
E_c	−2.756	−2.975[30]	−2.560[31]
Sr ($Fm\bar{3}m$)			
a_0	6.059	5.921[32]	6.040[33]
E_c	−1.774	−1.779[32]	−1.720[34]
Ba ($Im\bar{3}m$)			
a_0	5.067	4.887[35]	5.020[33]
E_c	−1.985	−2.052[35]	−1.900[34]
Ti ($P6_3/mmc$)			
a_0	2.932	2.931[36]	2.950[37]
c_0	4.653	4.670[36]	4.686[37]
E_c	−4.685	−5.450[36]	−4.850[34]
Zr ($P6_3/mmc$)			
a_0	3.160	3.178[32]	3.230[38]
c_0	5.134	5.126[32]	5.149[38]
E_c	−6.157	−6.925[32]	−6.250[36]

$$E_c = E_X^{stable-phase} - E_X^{atom} \tag{1}$$

In the case of oxygen, $E_X^{stable-phase}$ in eqn (1) is the total energy of a SCAN optimized O_2 dimer, which is simulated in a large asymmetric orthorhombic cell using only the Γ-point. On the other hand, $E_X^{stable-phase}$ values in the case of Sr, Ba, Ti and Zr are computed from their respective SCAN optimized crystal unit cells. E_X^{atom} in eqn (1) is the energy of an isolated single atom which has been computed by placing a single atom in an asymmetric orthorhombic unit cell using the Γ-point. For a correct determination of the $E_X^{stable-phase}$ and E_X^{atom} energies, spin-polarized calculations are adopted which ensure proper occupation.

It is evident from Tables 1 and 2 that the lattice parameters for elemental as well as binary solids obtained using the SCAN functional are in better agreement with experimental data compared to the GGA functional.[30–48] Importantly, the SCAN calculated values of E_c for Sr, Ba, Zr and Ti also a show significantly smaller deviation from experimental data which is usually much larger for semi-local DFT functionals.[13] Importantly, it is evident from our calculated values of bond length and cohesive energy for O_2 molecules that the SCAN functional does not suffer from the over-binding issue faced in other semi-local exchange–correlation energy functionals, thus providing an accuracy comparable to hybrid DFT calculations.[13,40,41] On the whole, better agreement of the structural properties[13] and cohesive energies of O_2 and elemental metals computed using SCAN with the experimental data (Table 1) clearly indicates that this meta-GGA exchange–correlation functional of DFT facilitates accurate determination of the thermodynamic properties of ABO_3 perovskite oxides.

As the primary result of a DFT calculation for solids is the determination of total energy, an important thermodynamic quantity that can be derived from the calculated total energy is the reaction energy, E_{React}, which plays an important role for identifying the application of the subject material in various technologies.[42] For the present study, E_{React} is the energy of perovskite oxides relative to cumulative energies of the binary oxides corresponding to the chemical reaction $AO + BO_2 \rightarrow ABO_3$. For this reason, we can compute E_{React} by subtracting the sum of total energies of its binary oxides AO (E_t^{AO}) and BO_2 $\left(E_t^{BO_2}\right)$ from the total energy of ABO_3 $\left(E_t^{ABO_3}\right)$ according to the relation[42]

$$E_{React} = E_t^{ABO_3} - \left(E_t^{AO} + E_t^{BO_2}\right) \tag{2}$$

However, since the total energies of ABO_3, AO and BO_2 compounds are also related to their respective enthalpies of formation by the formulas

$$\Delta H_f^{ABO_3} = E_t^{ABO_3} - E_A^{stable-phase} - E_B^{stable-phase} - 3\frac{1}{2}E_{O_2}^{stable-phase} \tag{3}$$

$$\Delta H_f^{AO} = E_t^{AO} - E_A^{stable-phase} - \frac{1}{2}E_{O_2}^{stable-phase} \tag{4}$$

and

$$\Delta H_f^{BO_2} = E_t^{BO_2} - E_B^{stable-phase} - 2\frac{1}{2}E_{O_2}^{stable-phase}, \tag{5}$$

respectively, we can see that E_{React} can also be expressed as

$$E_{React} = \Delta H_f^{ABO_3} - \left(\Delta H_f^{AO} - \Delta H_f^{BO_2}\right) \tag{6}$$

In the above equations, E_t is the total energy of the optimized unit cells of the concerned oxides. It is evident from eqn (2) to (6) that only a good determination of the ground state total energies of AO, BO_2 and ABO_3 would ensure accurate computation of E_{React}. For the present study, we have computed the ground state lattice parameters and enthalpies of formation of the relevant AO and BO_2 binary oxides using the SCAN meta-GGA functional, which are presented in Table 2. A comparison of the lattice parameters presented in Table 2 clearly shows that the SCAN functional gives a much better account of the structural properties of SrO, BaO, TiO_2 and ZrO_2 compared to the common semi-local functionals belonging to the first two rungs of the Jacob's ladder.[8] At the same time, the calculated enthalpies of the formation for the four AO and BO_2 oxides clearly show that large overestimation commonly seen in the GGA calculations is eliminated by the employment of the SCAN functional. This can mainly be ascribed to the fact that the SCAN functional does not suffer from the over-binding of oxygen bonds, which allows it to perform better for both molecules and solids.[13,23]

The lattice parameters of the ABO_3 (where A = Sr and Ba; B = Ti and Zr) compounds under consideration computed using the SCAN meta-GGA functional are presented in Table 3, while the total energy vs volume and pressure vs volume data are shown in Fig. 1. When compared to experimental data, the SCAN calculated lattice parameters of $SrTiO_3$ and $BaZrO_3$ are only slightly larger (<0.5%), while the lattice parameters for $BaTiO_3$ and $SrZrO_3$ are slightly smaller (<0.12%). It is also

Table 2 Lattice parameters (Å) and enthalpies of the formation (eV per f.u.) of cubic unit cell of strontium oxide, cubic unit cell of barium oxide, tetragonal unit cell of titania and monoclinic unit cell of zirconia computed using the SCAN functional. For the sake of comparison, results of the GGA functional reported in previous DFT studies and experimental data are also presented

Compound	SCAN (this work)	GGA (previous DFT studies)	Experiment
SrO ($Fm\bar{3}m$)			
a_0	5.163	5.128[32]	5.161[39]
ΔH_f	−6.079	−6.414[32]	−6.140[43]
BaO ($Fm\bar{3}m$)			
a_0	5.553	5.493[35]	5.539[44]
ΔH_f	−5.604	−5.967[35]	−5.680[43]
TiO_2 ($P42/mnm$)			
a_0	4.597	4.653[45]	4.590[46]
b_0	2.973	2.969[45]	2.956[46]
ΔH_f	−10.080	−10.425[45]	−9.740[46]
ZrO_2 ($P2_1c$)			
a_0	5.174	5.133[32]	5.151[47]
b_0	5.238	5.212[32]	5.203[47]
c_0	5.364	5.411[32]	5.316[47]
ΔH_f	−11.371	−12.117[32]	−11.410[48]

This journal is © The Royal Society of Chemistry 2021

J. Mater. Chem. C, 2021, **9**, 4862–4876 | **4865**

Table 3 Lattice parameters (Å) and enthalpies of the formation (eV per f.u.) of cubic perovskite unit cells of strontium titanate, barium titanate, strontium zirconates and barium zirconate computed using SCAN functional. For the sake of comparison, results of GGA reported in previous DFT studies and experimental data are also presented

Compound	SCAN (this work)	GGA (previous works)	Experiment
SrTiO$_3$			
a_0	3.909	3.943[50]	3.890[51]
ΔH_f	−17.533	−17.805[45]	−17.000[52]
BaTiO$_3$			
a_0	3.996	4.035[50]	4.000[51]
ΔH_f	−17.233	−17.435[45]	−17.265[52]
SrZrO$_3$			
a_0	4.149	4.198[45]	4.154[53]
ΔH_f	−17.994	−18.080[45]	−18.320[54]
BaZrO$_3$			
a_0	4.207	4.256[45]	4.190[55]
ΔH_f	−18.226	−18.240[45]	−18.270[54]

evident from Table 3 that the enthalpies of formation computed using the SCAN functional for ABO$_3$ compounds are in better agreement with experimental values compared to GGA. These results further confirm the superior performance of this meta-GGA functional in determining the thermodynamics of complex oxides. From Fig. 1, it can also be seen that the pressure *vs.* volume data computed using the Birch–Murnaghan's equations of state give a linear variation of pressure with volume for the

SCAN calculations. Since the mechanical properties of perovskite materials (discussed later) are strongly dependent on smooth variation of pressure *vs* volume of the unit cell, Fig. 1 already indicates good performance of the SCAN meta-GGA functional.[13] It is also worth pointing out here that the experimental enthalpies of the formation for the ABO$_3$ compounds are less than the sum of enthalpies of the formation of the concerned binary oxides (*i.e.* $\Delta H_f^{AO} + \Delta H_f^{BO_2}$), which indicates that the structure of the cubic perovskite oxides is energetically stable.[49] Since experimental studies have shown the existence of BaTiO$_3$ in the cubic phase,[51,52] our calculated values of the enthalpies of the formation of BaTiO$_3$, BaO and TiO$_2$ clearly satisfy $\Delta H_f^{BaTiO_3} \leq \Delta H_f^{BaO} + \Delta H_f^{TiO_2}$, showing that the SCAN meta-GGA functional has good agreement with experimental observations which have earlier been satisfied only through the use of the semi-empirically corrected GGA+U method.[42]

As mentioned earlier, determination of E_{React} for the chemical reaction AO + BO$_2$ → ABO$_3$ is important for determining the suitability of a perovskite oxide for various applications.[42] In addition, E_{React} computed using DFT have also been used to examine the suitability of one-step and two-step techniques for synthesizing novel ternary compounds.[5] In the case of compounds crystallizing in the perovskite structure, one can
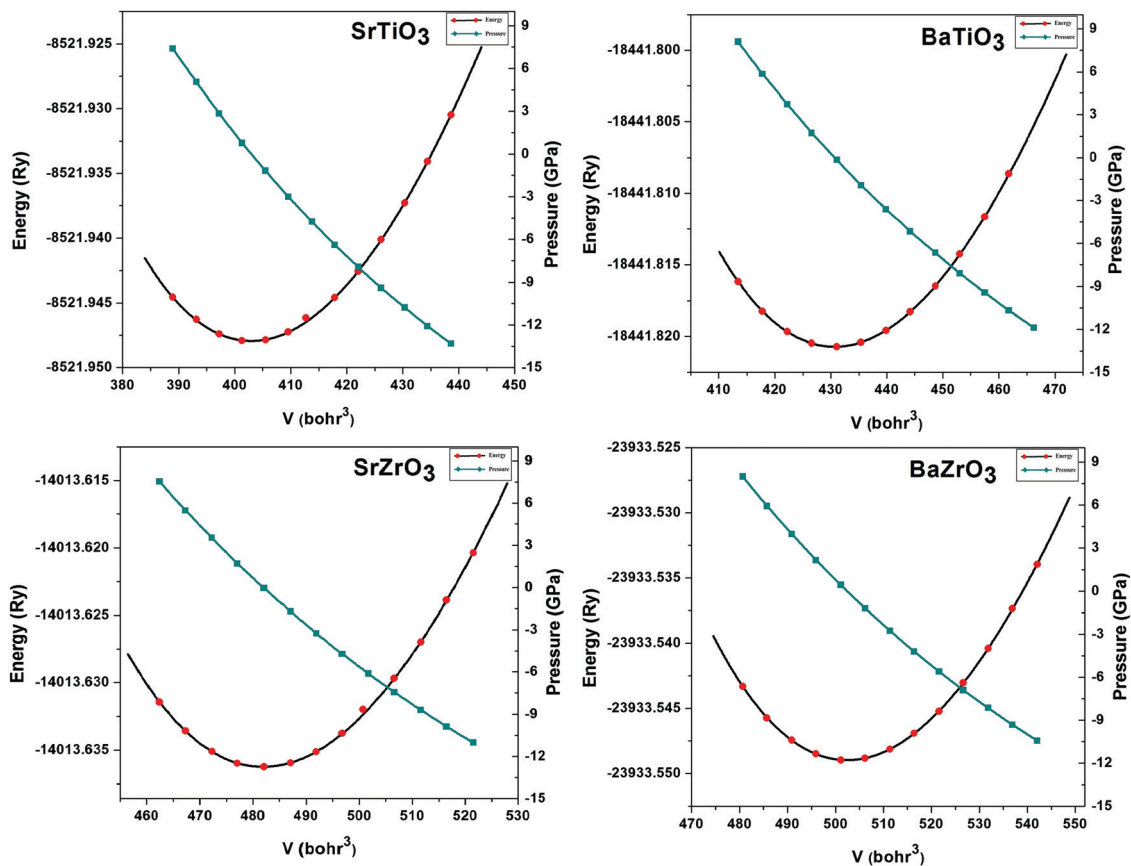

Fig. 1 The calculated total energy *vs.* volume and pressure *vs.* volume plots for SrTiO$_3$, BaTiO$_3$, SrZrO$_3$ and BaZrO$_3$ computed using the SCAN meta-GGA functional.

4866 | *J. Mater. Chem. C*, 2021, **9**, 4862–4876

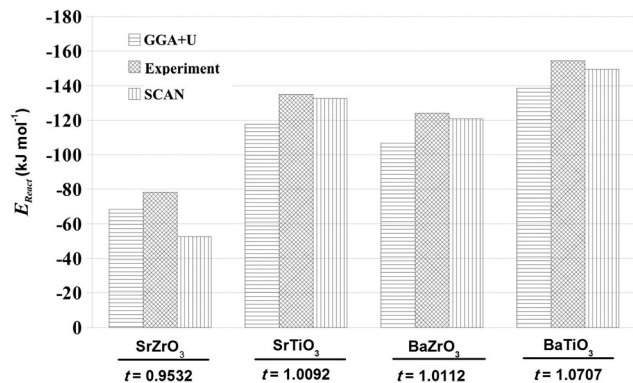This journal is © The Royal Society of Chemistry 2021

Fig. 2 The reaction energies, E_{React} (kJ mol^{-1}), for SrTiO$_3$, BaTiO$_3$, SrZrO$_3$ and BaZrO$_3$ plotted as a function of increasing Goldsmith tolerance factor, t. The GGA+U and experimental values are derived from data reported by Hautier et al.[42] and Kubaschewski et al.,[58] respectively.

relate E_{React} with the dimensionless Goldschmit's tolerance factor, t.[56] As the value of Goldschmit's tolerance factor indicates the stability of the perovskite structure, one expects an increase in t with increase in the values of E_{React}.[57] In Fig. 2 we present our SCAN calculated E_{React} values as a function of increasing t of the four perovskite oxides. The comparison of our calculated results with the previous GGA+U calculations[42] and experimental data[58] as shown in Fig. 2 makes it evident that the SCAN meta-GGA functional is efficient in predicting reaction energies. Importantly, the E_{React} values obtained for SrTiO$_3$, BaTiO$_3$ and BaZrO$_3$ with SCAN are found to be in excellent agreement with experimental ones.

3.2. Mechanical properties

Since the mechanical response of a material to applied forces can be derived from its elastic constants, DFT calculations are commonly employed to supplement experimental results[59] or to predict mechanical properties[60] of ABO$_3$ (where A = Sr and Ba; B = Ti and Zr) perovskite oxides. In the case of cubic crystals the mechanical properties can be completely defined in terms of three independent elastic constants C_{11}, C_{12} and C_{44}, which correspond to longitudinal compression, transverse expansion and shear elastic modulus, respectively.[61] Since the three elastic constants for cubic structure can be computed from straight forward total energy calculations, in the present study, we have used the SCAN meta-GGA functional to compute the elastic constants of the cubic perovskite structure of alkaline earth metal titanates and zirconates, which are presented in Table 4. The comparison of our SCAN results with previous GGA[59] calculations for SrTiO$_3$ reveals that both these functionals show small deviations from experimental data.[62] However, larger deviations of both SCAN and GGA results from the experimental data are evident in the case of BaTiO$_3$.[51] Since the large deviation of our calculated values of elastic constants for BaTiO$_3$ can be due to the fact that this compound generally adopts a distorted perovskite structure, it is difficult to judge the performance of SCAN functional based solely on the comparison between the data presented in Table 4.

Table 4 Elastic constants (GPa) of cubic perovskite unit cells of strontium titanate, barium titanate, strontium zirconates and barium zirconate computed using SCAN functional. For comparison GGA and experimental data are also presented where available

Compound	SCAN (this work)	GGA (previous works)	Experiment
SrTiO$_3$			
C_{11}	344.90	319.30[59]	317.20[62]
C_{12}	110.90	97.50[59]	102.50[62]
C_{44}	109.01	113.00[59]	123.50[62]
BaTiO$_3$			
C_{11}	310.34	310.40[59]	206.00[51]
C_{12}	113.67	107.20[59]	140.00[51]
C_{44}	130.21	139.80[59]	126.00[51]
SrZrO$_3$			
C_{11}	327.26	338.60[60]	—
C_{12}	78.32	71.00[60]	—
C_{44}	82.00	77.00[60]	—
BaZrO$_3$			
C_{11}	320.95	322.50[60]	—
C_{12}	84.22	79.00[60]	—
C_{44}	94.93	70.00[60]	—

Although various important mechanical parameters (e.g. shear modulus, Young's modules, Zener anisotropy factor, and Kleinman parameter) can be derived from C_{11}, C_{12} and C_{44} using simple mathematical formulas,[61] we note that only experimental data of elastic constants for SrTiO$_3$ and BaTiO$_3$ are available in the literature.[51,62] However, Yamanak et al.[63,64] have carried out studies for measuring the thermophysical properties of SrZrO$_3$ and BaZrO$_3$ in which they report the shear modulus, G (GPa), and Young's modulus, Y (GPa), of these perovskite oxides. For this reason, we first compute the bulk modulus, B (GPa), Voigt's shear modulus, S_V (GPa), and Reuss's shear modulus, S_R (GPa) for the four ABO$_3$ compounds using the formulas

$$B = \frac{1}{3}(C_{11} + 2C_{12}) \tag{7}$$

$$S_V = \frac{C_{11} - C_{12} + 3C_{44}}{5} \tag{8}$$

and

$$S_R = \frac{5}{\dfrac{4}{C_{11} - C_{12}} + \dfrac{3}{C_{44}}}, \tag{9}$$

respectively. The values computed using eqn (7) through (9) are subsequently used for computing G and Y from

$$G = \frac{S_V + S_R}{2} \tag{10}$$

and

$$Y = \frac{9GB}{G + 3B}, \tag{11}$$

respectively. On comparing our calculated values of G and Y with GGA and experimental data presented in Fig. 3, it is clear that the SCAN meta-GGA functional performs better than the semi-local GGA functionals for predicting the mechanical properties of perovskites considered in this work.
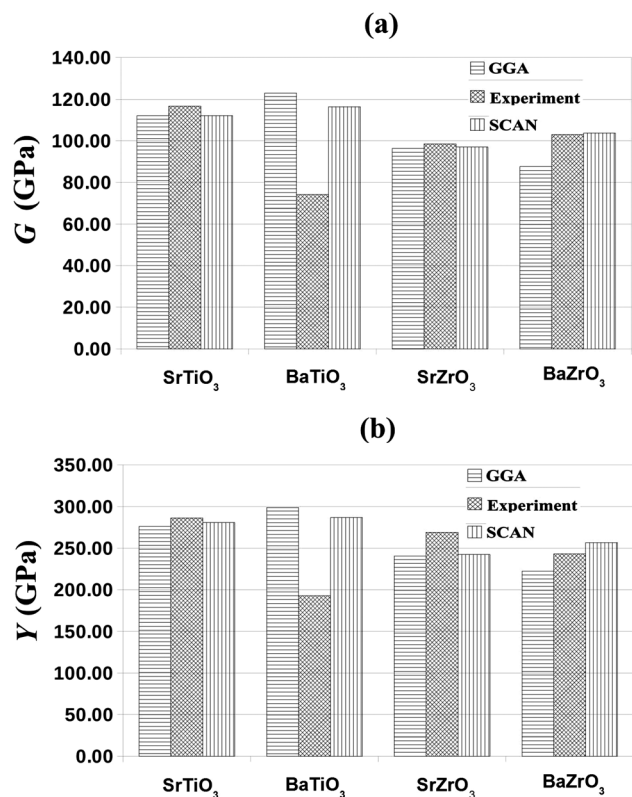
This journal is © The Royal Society of Chemistry 2021

J. Mater. Chem. C, 2021, **9**, 4862–4876 | **4867**

Fig. 3 The SCAN calculated shear modulus, G (GPa), and Young's modulus, Y (GPa), of $SrTiO_3$, $BaTiO_3$, $SrZrO_3$ and $BaZrO_3$ together with the GGA and experimental values reported in ref. 59, 60 and ref. 51, 62–64, respectively.

3.3. Vibrational properties

Vibrational properties of solids can be evaluated in terms of phonons that represent the collective dynamic excitations in a periodic lattice. Apart from being significantly important in indicating phase stability and structural transitions, phonons are crucial in modulating the transport properties of charge carriers in bulk[65–67] and nano-materials.[68,69] Since lattice vibrations can provide additional momentum to charge carriers of indirect band gap materials,[70] phonons also play a key role in interband transitions. For this reason, a reliable knowledge of the phonon modes in a perovskite photocatalyst can prove useful in designing improved absorption of electromagnetic radiations[71,72] as well as controlling the electron–hole recombination rates.[73,74] For the five atom cubic unit cell of the perovskites considered in this work, there are five triply degenerate phonons at the Brillouin zone center (Γ-point). Among these phonons, one of the triply degenerate phonons is acoustic while the remaining four are optical. The coherent movement of charges in the acoustic phonons gives them zero frequency at the Γ-point, while the four triply degenerate optical phonons in a cubic perovskite structure have non-zero frequencies at the Γ-point.[75] Three of these four triply degenerate optical phonons are infrared active and are designated as $\Gamma_{15}(TO1)$, $\Gamma_{15}(TO2)$ and $\Gamma_{15}(TO3)$; corresponding to A–BO_3 ferroelectric soft mode, O–B–O bend mode and B–O stretch mode, respectively.[75] On the other hand, the fourth triply

degenerate (designated as Γ_{25}) phonon mode is optically inactive and corresponds to a B–O_3 torsion mode.[75]

It is well know that the dielectric and ferroelectric properties of the cubic ABO_3 perovskite oxides are controlled by phonons,[51,53,55,76] which can be modified by varying the stress or temperature. It is therefore intuitive to assess the performance of a DFT functional in predicting experimentally observed phonon modes and instabilities (e.g. ferroelectric at low temperatures). Unfortunately, a correct description of the vibrational properties from the frozen phonon approximation using semi-local as well as advanced functionals of DFT at 0 K has remained a challenge.[50,77–81] For instance, plane wave (PW) based DFT calculations by Wahl et al.[50] utilizing both semi-local and Heyd–Scuseria–Ernzerhof (HSE06) schemes only confirm the experimentally observed Sr–TiO_3 ferroelectric soft mode of $SrTiO_3$ to be real within the LDA approximation (see Table 5). On the contrary, all of LDA, GGA and HSE06 confirm the imaginary Ba–TiO_3 ferroelectric soft mode of $BaTiO_3$.[50] However, recent employment of the SCAN functional for computing phonon modes of $SrTiO_3$ and $BaTiO_3$ at the Γ-point using the projector augmented wave (PAW) method has shown better performance of this meta-GGA exchange–correlation parameterization scheme.[79] Since the PW/PAW based DFT calculations of phonons for the considered class of compounds are found to be sensitive to the choice of pseudopotentials as well as the treatment of semi-core states as valence or core states,[79,80,82] an accurate all-electron account of vibrational frequencies at the Γ-point through FP-LAPW method of DFT using the SCAN meta-GGA functional is therefore mandated.

Since performance evaluation of various DFT functionals in predicting the vibrational properties of ABO_3 perovskites can be carried out on the basis of optical phonon frequencies at the Γ symmetry point,[50,75–78] in Table 5 we present our SCAN results together with the available earlier theoretical and experimental values. It is worth pointing out here that unlike the usual space group dependent unit cell calculations performed within the WIEN2k code for structural and electronic properties, the phonopy code requires forces caused by finite atomic displacements to be computed within supercells which are deprived of space group.[28] For this reason, in this work, the atomic forces for the 40-atom supercells have been computed using Γ-point sampling. From Table 5 it is evident that the Γ-point phonon frequencies computed using SCAN in the present FP-LAPW calculations are in excellent agreement with the available experimental data.[83–85] One can clearly see that both $SrTiO_3$ and $BaZrO_3$ show no tendency for ferroelectric distortion at low temperatures. On the other hand, both $BaTiO_3$ and $SaZrO_3$ show a tendency to ferroelectric distortions at low temperatures, which has also been observed in earlier studies.[50,82,84] It is particularly important to notice that our calculated values for $SrTiO_3$ and $BaTiO_3$ are in better agreement with the experimental data compared to HSE06.[50] Moreover, our FP-LAPW results of the A–BO_3 ferroelectric soft mode for $SrTiO_3$ and $BaZrO_3$ computed using SCAN are the closest to the experimental data when compared with earlier theoretical results.[79,82,83,85] The better performance of SCAN can mainly be attributed to the fact that an accurate determination of the vibrational properties using the

4868 | J. Mater. Chem. C, 2021, **9**, 4862–4876

This journal is © The Royal Society of Chemistry 2021

Table 5 The Γ-point optical phonon frequencies (THz) for the cubic phase of ABO$_3$ (where A = Sr and Ba; B = Ti and Zr) compounds computed using the SCAN meta-GGA functional in the present study compared with the available theoretical results computed using the SCAN, LDA, GGA and HSE06 functionals and experimental data. Imaginary frequencies are indicated by imaginary unit, i, after the value

Compound symmetry	DFT method-functional					Experiment
	FP-LAPW-SCAN	PW-SCAN	PW-LDA	PW-GGA	PW-HSE06	
SrTiO$_3$						
Γ_{15} (TO1)	2.811	2.398[79]	2.398[50]	3.448 i[50]	2.248 i[50]	2.749[83]
Γ_{15} (TO2)	5.060	5.186[79]	5.306[50]	4.407[50]	4.857[50]	5.066[83]
Γ_{25}	7.309	7.495[79]	6.774[50]	7.015[50]	7.495[50]	7.945[83]
Γ_{15} (TO3)	16.128	16.369[79]	16.878[50]	15.349[50]	15.979[50]	16.399[83]
BaTiO$_3$						
Γ_{15} (TO1)	4.532 i	6.595 i[79]	2.248 i[50]	3.837 i[78]	7.225 i[50]	—
Γ_{15} (TO2)	5.130	5.486[79]	5.786[50]	5.576[78]	5.546[50]	5.456[84]
Γ_{25}	8.733	8.694[79]	8.574[50]	8.454[78]	9.296[50]	9.237[84]
Γ_{15} (TO3)	14.022	14.270[79]	14.390[50]	14.060[78]	14.390[50]	14.450[84]
SrZrO$_3$						
Γ_{15} (TO1)	1.874 i	—	3.418[80]	2.608 i[82]	—	—
Γ_{15} (TO2)	6.074	—	6.446[80]	—	—	—
Γ_{25}	3.528	—	5.366[80]	—	—	—
Γ_{15} (TO3)	16.877	—	16.309[80]	—	—	—
BaZrO$_3$					—	
Γ_{15} (TO1)	2.883	—	2.878[81]	2.728[75]	—	3.448[85]
Γ_{15} (TO2)	5.961	—	5.786[81]	5.696[75]	—	6.296[85]
Γ_{25}	5.735	—	—	5.456[75]	—	—
Γ_{15} (TO3)	14.788	—	15.379[81]	14.480[75]	—	15.140[85]

frozen phonon approximation requires very precise computation of the curvature of the total energy surface with respect to the atomic displacements introduced in the solid. As SCAN already shows good performance in determining the total energy dependent physical properties of atoms, molecules and solids,[13] from Table 5 it is evident that it also performs better than the computationally expensive HSE06 functional in determining the vibrational properties of ABO$_3$ perovskites.[50,79]

3.4. Electronic properties

Using the lattice parameters optimized with the SCAN functional, we have computed the electronic density of states (DOS) and band structure diagrams of the selected alkaline earth metal titanates and zirconates, which are presented in Fig. 4 and 5, respectively. For these properties both SCAN and mBJ-LDA functionals are employed since the former DFT functional is known to underestimate the band gaps of solids despite its good performance for structural and energetic properties.[13,23] By comparing Fig. 4 and 5, one can see that the overall features of the electronic properties for SrTiO$_3$, BaTiO$_3$, SrZrO$_3$ and BaZrO$_3$ computed using the two meta-GGA functionals are similar. However, both the DOS and band structure diagrams show that the positioning of the electronic states belonging to conduction and valence bands computed using SCAN//mBJ-LDA simulations are modified, which results in increase of the band gaps. From Fig. 4 we can see that the upper valence bands for SrTiO$_3$ and BaTiO$_3$ are mainly composed of the O-2p states along with a minor contribution coming from the Ti-3d states. In a similar fashion, Fig. 5 shows that upper valence bands for SrZrO$_3$ and BaZrO$_3$ are mainly composed of the O-2p states along with a minor contribution coming from the Zr-4d states. Irrespective of the choice of the functional, it is also evident that for all the ABO$_3$ perovskites considered in this study the conduction band edge is mainly

composed of the B atom's d states along with a minor contribution coming from the O-2p states. Moreover, the contribution of Sr-5s and Ba-6s states in the conduction band minimum is negligible; however, these states dominate the conduction band at higher energies. This is understandable since the ABO$_3$ perovskite oxides are composed of alternating layers of AO and BO$_2$, such that stronger covalent bonding between B and O atoms dominates the conduction and valence band edges, respectively.[32,35]

From the electronic properties of ABO$_3$ (where A = Sr and Ba; B = Ti and Zr) shown in Fig. 4 and 5, it is evident that the fundamental energy band gap between the O-2p states at the valence band edge and the B atom's d states at the conduction band edge is along the $R \rightarrow \Gamma$ direction. On the other hand, the optical band gap for all these compounds is slightly larger than the fundamental band gap, which is along the $\Gamma \rightarrow \Gamma$ direction. The SCAN and mBJ-LDA calculated band gaps for ABO$_3$ (where A = Sr and Ba; B = Ti and Zr) along the $R \rightarrow \Gamma$ and $\Gamma \rightarrow \Gamma$ directions are presented in Table 6 and compared with earlier theoretical results computed using GGA and HSE06 functionals as well as with experimental data.[86–91] It is clear that the SCAN meta-GGA functional employed in this study underestimates band gaps for the perovskite oxides considered here, which are only slightly larger than the band gaps predicted by the GGA functional.[23,86,92] The comparison of the fundamental band gaps computed using SCAN//mBJ-LDA simulations and the ones computed using hybrid DFT in ref. 86 shows that a relatively smaller shift of the B atom's d states making up the conduction band edge at the Γ symmetry point is achieved with the meta-GGA (i.e. mBJ-LDA) functional employed here. Since the band structures shown in Fig. 4 and 5 reveal that the application of mBJ-LDA does not shift the O-2p states located at the R symmetry point, our calculated mBJ-LDA R $\rightarrow \Gamma$ band
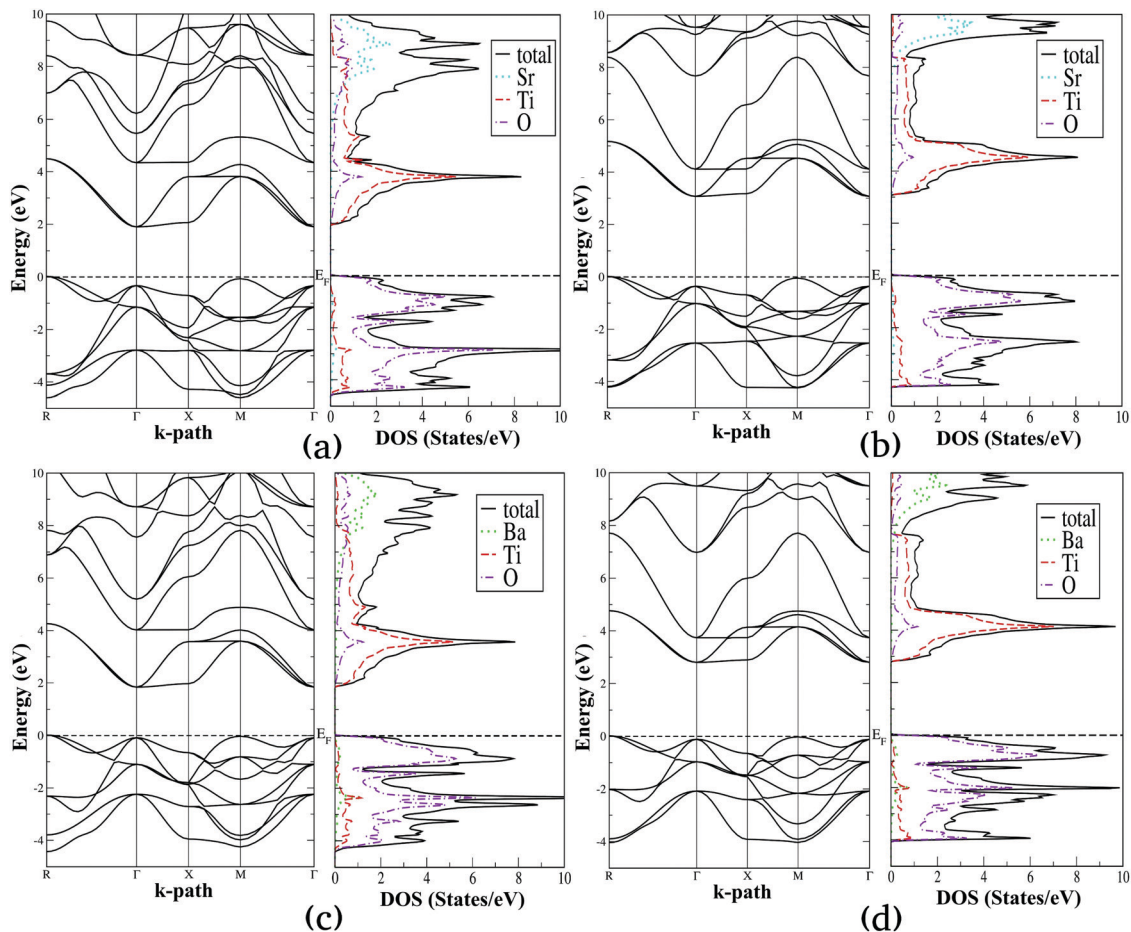
This journal is © The Royal Society of Chemistry 2021

J. Mater. Chem. C, 2021, **9**, 4862–4876 | **4869**

Fig. 4 Calculated electronic band structure diagrams and density of states plots for $SrTiO_3$ (a and b) and $BaTiO_3$ (c and d) computed using SCAN (a and c) and mBJ-LDA (b and d) meta-GGA functionals.

gaps are smaller than the ones obtained using the HSE06 functional.[86] On the other hand, Fig. 4 and 5 clearly show that the O-2p states located at the Γ symmetry point below the Fermi level are pushed towards more negative energies with the application of the mBJ-LDA functional. As a consequence, the optical band gaps of $SrTiO_3$ and $SrZrO_3$ computed using the SCAN//mBJ-LDA simulations (Table 6) are in better agreement with the experimental data.[87–91] On the other hand, optical band gaps of cubic $BaTiO_3$ and $BaZrO_3$ are slightly smaller when compared with the hybrid DFT results.[86] Despite the fact that different experimental values for the optical band gaps of $BaZrO_3$ are reported in the literature,[90,91] comparison of our calculated band gap with earlier works suggests that the performance of the mBJ-LDA functional for barium compounds is also satisfactory. In particular, the small difference in the fundamental and optical band gap of cubic $BaTiO_3$ (0.11 eV) is in good agreement with the previous experimental reports which reported difficulty in determining the direct or indirect nature of the band gap for this material.[88] Thus, our results allow us to claim that the SCAN//mBJ-LDA simulations are a better choice than HSE06 for reliably evaluating the optical properties and photocatalytic performance of ABO_3 (where A = Sr and Ba; B = Ti and Zr) perovskite oxides.

3.5. Optical properties

For practical purposes, the application of a material in optical devices can be directly related to its absorption properties. Since the optical band gaps of ABO_3 (where A = Sr and Ba; B = Ti and Zr) ceramics make them suitable for applications in devices operating in the 220 nm–360 nm wavelength range, it is intuitive to examine their optical properties. As a long range of absorption appears to be plausible for transition between states having varying degrees of spatial overlaps, the band gap alone does not give complete information of absorption properties. To address this issue, optical absorption in a wide range of wavelength has been obtained for $SrTiO_3$, $BaTiO_3$, $SrZrO_3$ and $BaZrO_3$ perovskite oxides by computing the real and imaginary parts of the complex dielectric function.[93,94] The optical absorption plots calculated using the SCAN and mBJ-LDA meta-GGA functionals are presented in Fig. 6. Irrespective of the choice of the functional used, it is evident that the optical absorption is maximum in the far-UV region (<200 nm) of the electromagnetic spectrum. Since the SCAN functional is unable to accurately reproduce the experimental band gaps of the compounds under study, one can see that the threshold of the optical absorption for this functional is in the visible region for the titanates and UV region for the zirconates. However, the
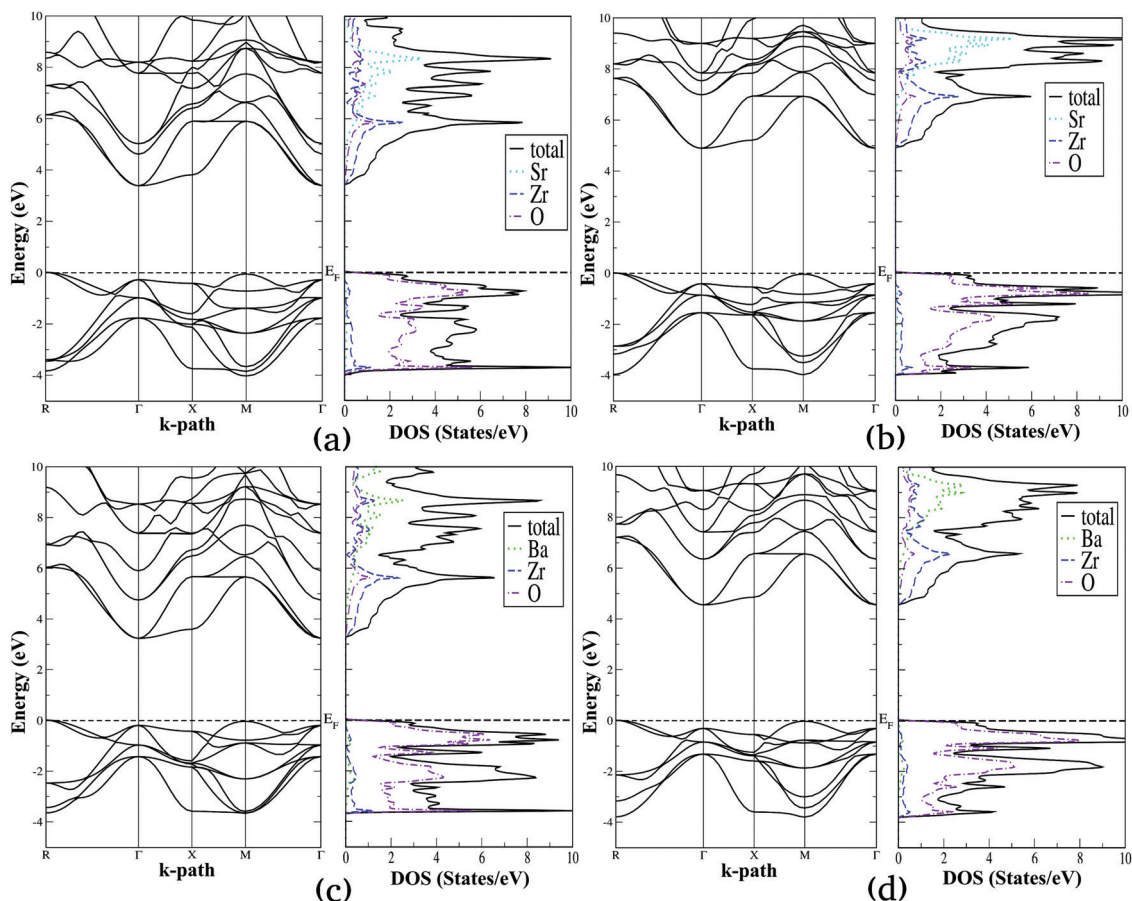
4870 | J. Mater. Chem. C, 2021, 9, 4862–4876

This journal is © The Royal Society of Chemistry 2021

Fig. 5 Calculated electronic band structure diagrams and density of states plots for SrZrO₃ (a and b) and BaZrO₃ (c and d) computed using SCAN (a and c) and mBJ-LDA (b and d) meta-GGA functionals.

Table 6 The calculated fundamental ($R \rightarrow \Gamma$) and optical ($\Gamma \rightarrow \Gamma$) band gaps (eV) of SrTiO₃, BaTiO₃, SrZrO₃ and BaZrO₃ perovskites computed using SCAN and mBJ-LDA meta-GGA functionals along with the GGA and HSE06 band gaps reported in a previous theoretical study and experimental data

	Fundamental band gap (along $R \rightarrow \Gamma$ direction)				Optical band gap (along $\Gamma \rightarrow \Gamma$ direction)				
	SCAN	mBJ-LDA	GGA	HSE06	SCAN	mBJ-LDA	GGA	HSE06	Experiment
SrTiO₃	1.90	3.07	1.87[86]	3.29[86]	2.23	3.42	2.24[86]	3.69[86]	3.43[87]
BaTiO₃	1.84	2.80	1.78[86]	3.14[86]	1.92	2.91	1.93[86]	3.27[86]	∼3.20[a 88]
SrZrO₃	3.38	4.89	3.44[86]	4.93[86]	3.65	5.30	3.68[86]	5.29[86]	5.60[89]
BaZrO₃	3.23	4.55	3.22[86]	4.67[86]	3.42	4.85	3.46[86]	4.99[86]	5.30,[90] 5.05[91]

[a] Temperature extrapolated value derived from optical band gap of tetragonal BaTiO₃.

results computed using SCAN//mBJ-LDA simulations show that the threshold of optical absorption for all the compounds under consideration is in the UV region, in agreement with the experimental observations.[87–91]

3.6. Photocatalytic performance

Despite the fact that the optical absorption plots shown in Fig. 6 indicate that SrTiO₃, BaTiO₃, SrZrO₃ and BaZrO₃ are suitable for applications in optical devices operating in the UV region of the electromagnetic spectrum, the application of these perovskite oxides for hydrogen production through photocatalysis requires that the band edge potentials are

appropriate with reference to water oxidation and reduction potentials.[16] It is well known that for successfully producing hydrogen by water splitting, a material's conduction band minima (CBM) should be more negative than the reduction potential of H⁺/H₂, while the valence band maxima (VBM) should be more positive than the oxidation potential of H₂O/O₂.[16] In order to estimate positions of the conduction and valence band edges of the compounds under study, we have computed band edge potential using the procedure detailed in ref. 95–98 for the SCAN, mBJ-LDA and experimental optical band gaps presented in Table 6. The calculated results are presented in Fig. 7, where one can see that the edge potential of CBM computed using

This journal is © The Royal Society of Chemistry 2021

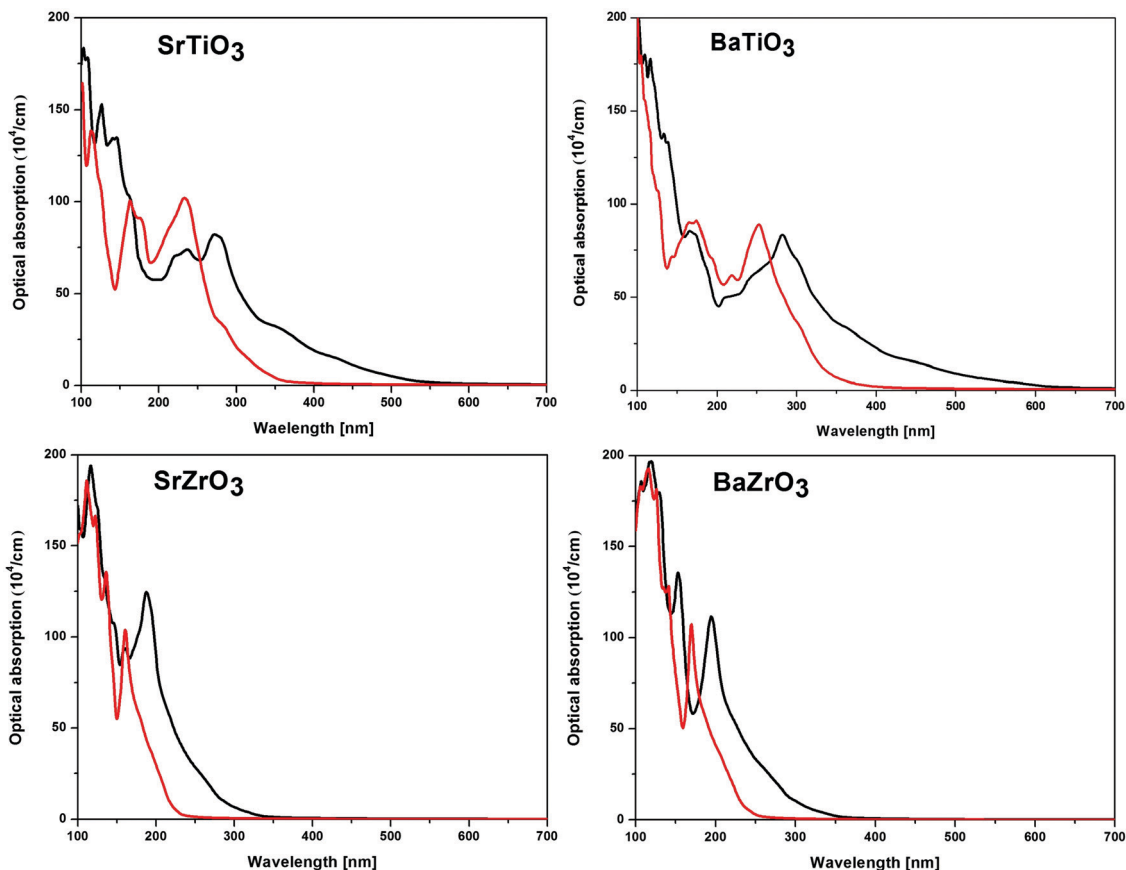*J. Mater. Chem. C*, 2021, **9**, 4862–4876 | **4871**

Fig. 6 The calculated optical absorption of SrTiO₃, BaTiO₃, SrZrO₃ and BaZrO₃ perovskite oxides computed using the SCAN (black line) and mBJ-LDA (red line) meta-GGA functionals.
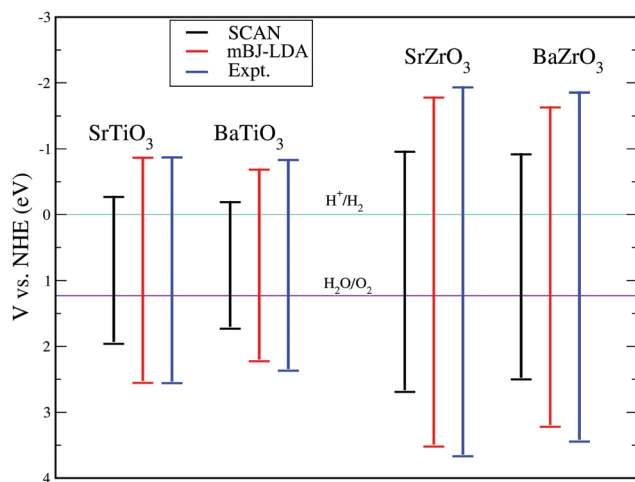

Fig. 7 The band edge potentials for SrTiO₃, BaTiO₃, SrZrO₃ and BaZrO₃ perovskite oxides calculated using the SCAN, mBJ-LDA and experimental optical band gaps.[87–91]

SCAN//mBJ-LDA simulations is located −0.89 eV, −0.71 eV, −1.81 eV and −1.66 eV above the reduction potential of water for SrTiO₃, BaTiO₃, SrZrO₃ and BaZrO₃, respectively. On the other hand, the band edge potentials of VBM for SrTiO₃, BaTiO₃, SrZrO₃ and BaZrO₃ computed using SCAN//mBJ-LDA simulations are

found to be 2.53 eV, 2.20 eV, 3.49 eV and 3.20 eV below the oxidation potential of water, respectively. A comparison of the results presented in Fig. 7 again makes it evident that the mBJ-LDA functional is able to provide better agreement with experiment as compared to the SCAN functional.

An important feature evident from our calculated mBJ-LDA results and experimental data presented in Fig. 7 is that the Ti based compounds have both their CBM and VBM edge potentials located close to the H⁺/H₂ and H₂O/O₂ potentials, respectively, when compared to the Zr based compounds. Since reports from 1980s already show insignificant photocatalytic activity of pristine SrTiO₃ for splitting water,[99,100] one might suspect that pristine perovskite oxides with band gap > 4 eV (e.g. LiTaO₃[101] and BaZrO₃[102]) are more suited for hydrogen production. However, this is not the case, because SrTiO₃ loaded with a co-catalyst show an improved photocatalytic activity. This is due to the lower rate of recombination of the photogenerated electron and holes achieved in Rh loaded SrTiO₃, which results in better hydrogen evolution (628 μmol h⁻¹)[103] when compared to pristine BaZrO₃ (104.5 μmol h⁻¹).[102] Therefore, recombination is an important factor influencing the photocatalytic performance of a material[104] that can be evaluated in terms of the transfer rate of photogenerated electrons and holes in the reduction and oxidation processes.[105] Unfortunately, the transfer rate of photogenerated electrons and

4872 | J. Mater. Chem. C, 2021, 9, 4862–4876

This journal is © The Royal Society of Chemistry 2021

Table 7 The electron and hole effective masses (in units of free electron mass m_e) corresponding to the curvatures of conduction band at Γ point and curvature of valence band along R point, respectively, along with ratios of m_e^* and m_h^* computed using the SCAN and mBJ-LDA meta-GGA functionals

Compound	SCAN			mBJ-LDA		
	$m_e^* \ \Gamma \rightarrow R$	$m_h^* \ R \rightarrow \Gamma$	D	$m_e^* \ \Gamma \rightarrow R$	$m_h^* \ R \rightarrow \Gamma$	D
$SrTiO_3$	0.80	−2.36	2.95	1.07	−2.70	2.53
$BaTiO_3$	0.83	−2.34	2.82	1.10	−2.69	2.44
$SrZrO_3$	0.60	−2.47	4.14	0.71	−2.87	4.03
$BaZrO_3$	0.59	−2.42	4.08	0.70	−2.82	4.01

holes cannot be directly measured from DFT calculations, however, it can indirectly be evaluated from the absolute ratio of the effective masses of the photogenerated holes and electrons

$$m_{h/e}^* = \frac{\hbar^2}{\frac{d^2 E_k}{dk^2}} \tag{12}$$

in valence and conduction bands, respectively, according to the formula[105]

$$D = \left| \frac{m_h^*}{m_e^*} \right| \tag{13}$$

A large value of D would indicate a better transfer rate of photogenerated electrons and holes, hence lower rate of recombination. On the other hand, smaller values of D would indicate higher rate of recombination. In eqn (12), E_k is the energy corresponding to wavevector k. Since the fundamental band gaps of Ti and Zr based perovskite oxides considered in this work are along the $R \rightarrow \Gamma$ symmetry points, we have considered the curvatures of the bands at Γ point for computing the effective mass of electron and the curvatures of the bands at R point for computing the effective mass of holes.[105] A comparison of the results computed using SCAN and mBJ-LDA (Table 7) clearly indicates that effective masses obtained from the former meta-GGA functional are slightly smaller; indicating that SCAN gives a larger curvature for both the conduction and valence band edges. This inability of the SCAN functional in predicting the accurate band structures of materials having band gaps > 1 eV is analogous to the results obtained with a GGA functional[23] which also results in an underestimation of the effective masses.[106] On the contrary, application of mBJ-LDA causes narrowing of the band dispersion that results in large effective masses, which are overestimated as compared to experimental data.[106,107] Nevertheless, the values of D computed using both the SCAN and mBJ-LDA functionals clearly show that an improved separation of charges should be expected from Zr based perovskite oxides. These results are in accordance with the photocatalytic hydrogen evolution under UV irradiation of pristine $SrTiO_3$[99,100] and $BaZrO_3$.[102] We therefore conclude that the employment of SCAN//mBJ-LDA simulations for investigating oxide semiconductors using DFT allows a reliable account of the structural, electronic and photocatalytic properties which are usually possible through computationally expensive hybrid functionals or GW methods.[13,14] Moreover, our results clearly suggest that the employment of a combination of SCAN and mBJ-LDA meta-GGA functionals for examining the modulation of band edge potentials of large band gap ceramics by means of doping can be important in predicting new photocatalysts.

4. Conclusions

In conclusions, we have performed a systematic analysis of combined application of SCAN and mBJ-LDA meta-GGA functionals for computing the physical properties of alkaline earth metal titanate and zirconate in cubic perovskite structure using the FP-LAPW method of DFT. The potential of these perovskite oxides for photocatalytic hydrogen production by splitting water is also examined. Our results clearly show that the experimentally observed structural, energetic, mechanical and vibrational properties of large band gap perovskite oxides are accurately predicted by the SCAN functional. In particular, the accurate prediction of the structural and energetic properties of atomic species and the binary oxides involved in synthesis of the concerned perovskite oxides shows that SCAN meta-GGA functional is able to provide an accuracy comparable to that of hybrid DFT calculations. The comparison of SCAN calculated reaction energies for $SrTiO_3$, $BaTiO_3$, $SrZrO_3$ and $BaZrO_3$ shows good agreement with experimental observations, which have previously been achieved through GGA+U calculations. By computing the elastic constants and frequencies of the optical phonons at the Brillouin zone center of the concerned perovskite oxides, we also show that SCAN functional performs better than the semi-local GGA as well as HSE06 functional for accurately predicting the mechanical and vibrational properties of these materials. Despite its good performance for the above-mentioned physical properties of perovskite oxides, SCAN functional is found to fall short of reproducing the experimentally observed band gaps of alkaline earth metal titanates and zirconates. To address this issue, we show that the application of SCAN//mBJ-LDA simulations allows one to achieve better accuracy in determining the optoelectronic properties of $SrTiO_3$, $BaTiO_3$, $SrZrO_3$ and $BaZrO_3$. In agreement with experiments, all four compounds are found to be indirect band gap materials showing absorption thresholds in the UV region of the electromagnetic spectrum. Using the electronic band gaps predicted by mBJ-LDA meta-GGA functional we also show that our *ab initio* predicted band edge potentials and effective masses of photogenerated electrons and holes are consistent with photocatalytic hydrogen evolution observed in $SrTiO_3$ and $BaZrO_3$. Since *ab initio* calculations provide the means to simulate changes in material's properties, our results clearly demonstrate that combining SCAN and mBJ-LDA functionals of DFT would prove useful as a computationally economical and robust technique for designing new photocatalysts based on Ti and Zr based perovskite oxides. This can particularly prove useful in future DFT studies for exploring the

This journal is © The Royal Society of Chemistry 2021

J. Mater. Chem. C, 2021, **9**, 4862–4876 | **4873**

surface properties of photocatalysts where hybrid functionals become impractical owing to their huge computational costs.

Author contributions

Waqas Zulfiqar: Conceptualization, data curation, and writing – original draft. Syed Muhammad Alay-e-Abbas: Conceptualization, writing – original draft, validation, and supervision. Ghulam Abbas: Formal analysis and validation. Amel Laref: Validation and visualization. J. Andreas Larsson: Writing – review & editing, supervision, and validation. Ali Shaukat: Writing – review & editing and supervision.

Conflicts of interest

There are no conflicts to declare.

Acknowledgements

References

1 P. Hohenberg and W. Kohn, *Phys. Rev.*, 1964, **136**, B864.
2 W. Kohn and J. J. Sham, *Phys. Rev.*, 1965, **140**, A1133.
3 K. Burke, *J. Chem. Phys.*, 2012, **136**, 150901.
4 A. Jain, Y. Shin and K. A. Persson, *Nat. Rev. Mater.*, 2016, **1**, 15004.
5 P. Canepa, S. H. Bo, G. S. Gautam, B. Key, W. D. Richard, T. Shi, Y. Tian, Y. Wang, J. Li and G. Ceder, *Nat. Commun.*, 2017, **8**, 1759.
6 N. Mardirossian and M. Head-Gordon, *Mol. Phys.*, 2017, **15**, 2315.
7 N. Mardirossian and M. Head-Gordon, *J. Chem. Phys.*, 2015, **142**, 074111.
8 J. P. Perdew, A. Ruzsinszky, J. Tao, V. N. Staroverov, G. E. Scuseria and G. I. Csonka, *J. Chem. Phys.*, 2005, **123**, 062201.
9 F. Tran, J. Stelzl and P. Blaha, *J. Chem. Phys.*, 2016, **144**, 204120.
10 D. M. Ceperley and B. J. Alder, *Phys. Rev. Lett.*, 1980, **45**, 566–569.
11 J. P. Perdew, K. Burke and M. Ernzerhof, *J. Phys. Rev. Lett.*, 1996, **77**, 3865–3868.
12 B. G. Janesko, T. M. Henderson and G. E. Scuseria, *Phys. Chem. Chem. Phys.*, 2009, **11**, 443–454.
13 J. Sun, A. Ruzsinszky and J. P. Perdew, *Phys. Rev. Lett.*, 2015, **15**, 036402.
14 F. Tran and P. Blaha, *Phys. Rev. Lett.*, 2009, **102**, 226401.
15 A. Fujishima and K. Honda, *Nature*, 1972, **238**, 37–38.
16 J. Xing, W. Q. Fang, H. J. Zhao and H. G. Yang, *Chem. – Asian J.*, 2012, **7**, 642–657.
17 N. Dehnhardt, H. Borkowski, J. Schepp, R. Tonner and J. Heine, *Inorg. Chem.*, 2018, **57**, 633–640.
18 S. Zlotnik, D. M. Tobaldi, P. Seabra, J. A. Labrincha and P. M. Vilarinho, *Chem. Phys. Chem.*, 2016, **17**, 3570–3575.
19 H. Iwahara, T. Yajima, T. Hibino and H. Ushida, *J. Electrochem. Soc.*, 1993, **140**, 1687.
20 T. Yajima, K. Koide, H. Takai, N. Fukatsu and H. Iwahara, *Solid State Ionics*, 1995, **79**, 333–337.
21 U. De, K. R. Sahu and A. De, *Solid State Phenom.*, 2015, **232**, 235–278.
22 P. Kovács, F. Tran, P. Blaha and G. K. H. Madsen, *J. Chem. Phys.*, 2019, **150**, 164119.
23 G. S. Gautam and E. A. Carter, *Phys. Rev. Mater.*, 2018, **2**, 095401.
24 J. Muscat, A. Wander and N. M. Harrison, *Chem. Phys. Lett.*, 2001, **342**, 397–401.
25 P. Borlido, T. Aull, A. W. Huran, F. Tran, M. A. L. Marques and S. Botti, *J. Chem. Theory Comput.*, 2019, **10**, 5069–5079.
26 P. Blaha, K. Schwarz, G. Madsew, D. Kvasnicka and J. Luitz, WIEN2k: An Augmented Plane Wave Plus Local Orbital Program, Vienna University of Technology, Austria, 2014.
27 D. Koller, F. Tran and P. Blaha, *Phys. Rev. B: Condens. Matter Mater. Phys.*, 2012, **85**, 155109.
28 A. Togo and I. Tanaka, *Scr. Mater.*, 2015, **108**, 1–5.
29 J. M. Skelton, D. Tiana, S. C. Parker, A. Togo, I. Tanaka and A. Walsh, *J. Chem. Phys.*, 2015, **143**, 064710.
30 F. Tran, R. Laskowski, P. Blaha and K. Schwarz, *Phys. Rev. B: Condens. Matter Mater. Phys.*, 2007, **75**, 115131.
31 K. P. Huber, *Molecular spectra and molecular structure: IV. Constants of diatomic molecules*, Spr. Sci. & Bus. Med., 2013.
32 S. M. Alay-e-Abbas, M. W. Yousaf, G. Abbas, N. Amin and A. Laref, *Ceram. Int.*, 2019, **45**, 18281–18290.
33 M. S. Anderson, C. A. Swenson and D. T. Peterson, *Phys. Rev. B: Condens. Matter Mater. Phys.*, 1990, **41**, 3329.
34 C. Kittel and P. McEuen, *Introduction to solid state physics*, Wiley, New York, 2005, p. 105.
35 S. M. Alay-e-Abbas, F. Javed, G. Abbas, N. Amin and A. Laref, *J. Phys. Chem. C*, 2019, **123**, 6044–6053.
36 P. Janthon, S. Luo, S. M. Kozlov, F. Vines, J. Limtrakul, D. G. Truhlar and F. Illas, *J. Chem. Theory Comput.*, 2014, **10**, 3832.
37 G. Chiarotti, *Interaction of Charged Particles and Atoms with Surfaces*, LandoltBornstein-Group III Condensed Matter. Spr. Ber. Heid. 24c 1995.
38 J. Donohue, *The Structures of the Elements*, Wiley, New York, 1974, p. 191.
39 M. C. Verbraeken, E. Suard and J. T. Irvine, *J. Mater. Chem.*, 2009, **19**, 2766–2770.
40 J. Rogal, PhD thesis, Freie Universität, Berlin, 2006.

4874 | *J. Mater. Chem. C*, 2021, **9**, 4862–4876

This journal is © The Royal Society of Chemistry 2021

41 L. Schimka, J. Harl and G. Kresse, *J. Chem. Phys.*, 2011, **134**, 024116.

42 G. Hautier, S. P. Ong, A. Jain, C. J. Moore and G. Ceder, *Phys. Rev. B: Condens. Matter Mater. Phys.*, 2012, **85**, 155208.

43 M. W. Chase Jr., NIST-JANAF Thermochemical Tables, 4th edn, J. Phys. Chem. Ref. Data 4 (1998) 9.

44 L. G. Liu and W. A. Bassett, *J. Geophys. Res.*, 1972, **77**, 4934.

45 A. Jain, S. P. Ong, G. Hautier, W. Chen, W. D. Richards, S. Dacek, S. Cholia, D. Gunter, D. Skinner, G. Ceder and K. A. Persson, *APL Mater.*, 2013, **1**, 011002.

46 G. V. Samsonov, *The Oxide Handbook IFI*, Plenum, New York, 1982.

47 R. E. Hann, P. R. Suitch and J. L. Pentecost, *J. Am. Ceram. Soc.*, 1985, **68**, 285.

48 J. G. Speight, *Lange's Handbook of Chemistry*, McGrawHill, New York, 6 2005.

49 D. R. Lide, *CRC Handbook of Chemistry and Physics*. CRC Press, Boca Raton, 2007.

50 R. Wahl, D. Vogtenhuber and G. Kresse, *Phys. Rev. B: Condens. Matter Mater. Phys.*, 2008, **78**, 104116.

51 K. H. Hellwege and A. M. Hellwege, *Ferroelectrics and Related Substances, New Series, Landolt-Bornstein*, Springer Verlag, Berlin, vol. 3 1969.

52 O. Kubaschewski, C. B. Alcock and P. J. Spencer, *Materials Thermochemistry*, Pergamon, New York, vol. 6, 1993, p. 257.

53 B. J. Kennedy, C. J. Howard and B. C. Chakoumakos, *Phys. Rev. B: Condens. Matter Mater. Phys.*, 1999, **59**, 4023.

54 M. E. Huntelaar, A. S. Booij and E. H. P. Cordfunke, *J. Chem. Thermodyn.*, 1994, **26**, 1095.

55 W. Pies and A. Weiss, *Simple Oxocompounds of Zirconium (Oxozirconates); K.-H. Hellwege, A. M. Hellwege*, Springer Materials, New York, 1976.

56 V. M. Goldschmidt, *Die Naturwissen*, 1926, **21**, 477.

57 S. Stølen, *Chemical thermodynamics of materials*. John Wiley & Sons, New York 2005.

58 O. Kubaschewski, C. B. Alcock and P. J. Spencer, *Materials Thermochemistry*, Pergamon, New York, 1993, pp. 257–323.

59 S. Piskunov, *Comput. Mater. Sci.*, 2004, **29**, 165–178.

60 R. Terki, H. Feraoun, G. Bertrand and H. Aourag, *Phys. Status Solidi B*, 2005, **242**, 1054–1062.

61 C. Kittel, *Introduction to Solid State Physics*, John Wiley & Sons, Inc., USA, 1996.

62 R. O. Bell and G. Rupprecht, *Phys. Rev.*, 1963, **129**, 90.

63 J. S. Yamanaka, *J. Am. Ceram. Soc.*, 2005, **88**, 1496–1499.

64 S. Yamanaka, H. Fujikane, T. Hamaguchi, H. Muta, T. Oyama, T. Matsuda, S. Kobayashi and K. Kurosaki, *J. Alloys Compd.*, 2003, **359**, 109–113.

65 J. S. Kang, M. Li, H. Wu, H. Nguyen and Y. Hu, *Science*, 2018, **361**, 575–578.

66 J.-J. Zhou, O. Hellman and M. Benardi, *Phys. Rev. Lett.*, 2018, **121**, 226603.

67 Y. Kang and S. Han, *Phys. Rev. Appl.*, 2018, **10**, 044013.

68 K. Kaasbjerg, K. S. Thyhesen and K. W. Jaconbsen, *Phys. Rev. B: Condens. Matter Mater. Phys.*, 2012, **85**, 115317.

69 B. Liao, J. Zhou, B. Qiu, M. S. Dresselhaus and G. Chen, *Phys. Rev. B: Condens. Matter Mater. Phys.*, 2015, **91**, 235419.

70 J. Noffsinger, E. Kioupakis, C. G. Van de Walle, S. G. Louie and M. L. Cohen, *Phys. Rev. Lett.*, 2012, **108**, 167402.

71 X. Gong, O. Voznyy, A. Jain, W. Liu, R. Sabatini, Z. Piontkowski, G. Walters, G. Bappi, S. Nokhrin, O. Bushuyev, M. Yuan, R. Comin, D. McCamant, S. O. Kelley and E. H. Sargent, *Nat. Mater.*, 2018, **17**, 550–556.

72 T. Ghosh, S. Aharon, L. Etgar and S. Ruhman, *J. Am. Chem. Soc.*, 2017, **139**, 18262–18270.

73 J. He, A. S. Vasenko, R. Long and O. V. Prezhdo, *J. Phys. Chem. Lett.*, 2018, **9**, 1872–1879.

74 L. Cheng, C. Zhang and Y. Liu, *JPhys Mater.*, 2019, **2**, 045005.

75 P. G. Sundell, M. E. Björketun and G. Wahnström, *Phys. Rev. B: Condens. Matter Mater. Phys.*, 2006, **73**, 104112.

76 R. Schafranek, J. D. Baniecki, M. Ishii, Y. Kotaka, K. Yamanka and K. Kurihara, *J. Phys. D: Appl. Phys.*, 2012, **45**, 055303.

77 R. D. King-Smith and D. Vanderbilt, *Phys. Rev. B: Condens. Matter Mater. Phys.*, 1994, **49**, 5828–5844.

78 D. I. Bilc, R. Orlando, R. Shaltaf, G.-M. Rignanese, J. Íñiguez and P. Ghosez, *Phys. Rev. B: Condens. Matter Mater. Phys.*, 2008, **77**, 165107.

79 Y. Zhang, J. Sun, J. P. Perdew and X. Wu, *Phys. Rev. B*, 2017, **96**, 03514.

80 R. Vali, *J. Phys. Chem. Solids*, 2008, **69**, 876–879.

81 A. R. Akbarzadeh, I. Kornev, C. Malibert, L. Bellaiche and J. M. Kiat, *Phys. Rev. B: Condens. Matter Mater. Phys.*, 2005, **72**, 205104.

82 S. Amisi, E. Bousquet, K. Katcho and P. Ghosez, *Phys. Rev. B: Condens. Matter Mater. Phys.*, 2012, **85**, 064112.

83 W. G. Stirling, *J. Phys. C*, 1972, **5**, 2711–2730.

84 Y. Luspin, J. L. Servoin and F. Gervais, *J. Phys. C*, 1980, **13**, 3761–3773.

85 C. H. Perry, D. J. McCarthy and G. Rupprecht, *Phys. Rev.*, 1965, **138**, A1537.

86 M. Schlipf, PhD thesis, Forschungszentrum Jülich, 2013.

87 H. Dittrich, N. Karl, H. W. Schock and S. Kuck, *Ternary Compounds, Organic Semiconductors: Supplement*, Springer, 2000.

88 S. H. Wemple, *Phys. Rev. B: Solid State*, 1970, **2**, 2679.

89 Y. S. Lee, J. S. Lee, T. W. Noh, D. Y. Byun, K. S. Yoo, K. Yamaura and E. Takayama-Muromachi, *Phys. Rev. B: Solid State*, 2003, **67**, 113101.

90 J. Robertson, *J. Vac. Sci. Technol., B: Microelectron. Nanometer Struct.–Process., Meas., Phenom.*, 2000, **18**, 1785–1791.

91 H. Zhang, J. Qiao, G. Li, S. Li, G. Wang, J. Wang and Y. Song, *Ultrason. Sonochem.*, 2018, **42**, 356.

92 G. S. Gautam, T. P. Senftle and E. A. Carter, *Chem. Mater.*, 2018, **30**, 4543.

93 F. Wooten, *Optical properties of solids*, Academic Press, New York, 1972.

94 C. Ambrosch-Draxl and J. O. Sofo, *Comput. Phys. Commun.*, 2006, **175**, 1.

95 S. Akhtar, S. M. Alay-e-Abbas, G. Abbas, M. I. Arshad, J. Batool and N. Amin, *J. Appl. Phys.*, 2018, **123**, 161569.

This journal is © The Royal Society of Chemistry 2021

J. Mater. Chem. C, 2021, **9**, 4862–4876 | **4875**

96 M. A. Butler and D. S. Ginley, *J. Electrochem. Soc.*, 1978, **125**, 228.

97 Y. Xu and M. A. Schoonen, *Am. Miner.*, 2000, **85**, 543–556.

98 H. L. Zhuang and R. G. Hennig, *Phys. Rev. B: Condens. Matter Mater. Phys.*, 2013, **88**, 115314.

99 K. Domen, S. Naito, M. Soma, T. Onishi and K. Tamaru, *J. Chem. Soc., Chem. Commun.*, 1980, **12**, 543–544.

100 J. M. Lehn, J. P. Sauvage and R. Ziessel, *Nouv. J. Chim.*, 1980, **4**, 623–627.

101 A. Kudo, *Catal. Surv. Asia*, 2003, **7**, 31–38.

102 Y. Yuan, X. Zhang, L. Liu, X. Jiang, J. Lv, Z. Li and Z. Zou, *Int. J. Hydrogen Energy*, 2008, **33**, 5941–5946.

103 J. M. Lehn, J. P. Sauvage, R. Ziessel and L. Hilaire, *Isr. J. Chem.*, 1982, **22**, 168–172.

104 K. Ozawa, M. Emori, S. Yamamoto, R. Yukawa, S. Yamamoto, R. Hobara, K. Fujikawa, H. Sakama and I. Matsuda, *J. Phys. Chem. Lett.*, 2014, **5**, 1953–1957.

105 X. Meng, N. Yun and Z. Zhang, *Can. J. Chem. Eng.*, 2019, **97**, 1982–1998.

106 Y. S. Kim, M. Marsman and G. Kresse, *Phys. Rev. B: Condens. Matter Mater. Phys.*, 2010, **82**, 205212.

107 B. Traoré, G. Bouder, W. Lafargue-Dit-Hauret, X. Rocquefelte, C. Katan, F. Tran and M. Kepenekian, *Phys. Rev. B*, 2019, **99**, 035139.

4876 | *J. Mater. Chem. C*, 2021, **9**, 4862–4876

This journal is © The Royal Society of Chemistry 2021